Inspecting Stellar Angular Momentum Evolution and Ages using High-Resolution Spectroscopy

A Senior Research Thesis

Presented in Partial Fulfillment of the Requirements for graduation *with research distinction* in Astronomy in the undergraduate colleges of The Ohio State University

by

Maria Pudoka

The Ohio State University
April 2021

Project Adviser: Dr. Donald Terndrup, Department of Astronomy

Abstract

This thesis serves as a project report on an effort to analyze spectroscopic rotation rates of field stars and low-mass stars in the Alpha Persei open cluster to extract information about stellar ages from spectroscopic measures alone. A sample of unevolved G and K field dwarfs from Kim et al. (2016), of which we have high-resolution spectra, is combined with two large spectroscopic surveys from Brewer et al. (2016) and Buder et al. (2019) to explore three indicators of youth – rotation, lithium abundance, and kinematics. The stars chosen for the analysis reside on the main sequence below the luminosities where isochrone fitting can determine stellar ages. However, using parallaxes and proper motions retrieved from Gaia DR2, we show that, regardless of the selection methods in these samples, stars with detectable projected rotation ($\geq 6\,\mathrm{km\,s^{-1}}$) and lithium abundances are members of kinematically cold populations as expected of young stars. Using stellar evolution models from Denissenkov et al. (2010), we show that, with 90% confidence, a probabilistic upper limit for age may be assigned to a star with a given rotation rate. We pay particular attention to the effect of binarity and uncertainties in $v \sin i$ on the calculation of the age posteriors. We demonstrate errors in $v \sin i$ are not significant compared to the effects of inclination angle except when $v \sin i$ is at or near the detection limit. Finally, we discuss how well this method can be implemented to identify the youngest exoplanet host stars from spectra alone.

Contents

1 Introduction

1.1 Background and Motivation

The basic questions of this thesis were inspired by a paper published in 2016 by Kim et al.. In that analysis, the anomalous Hipparcos parallaxes for the Pleiades cluster were analyzed by searching for subluminous field stars as would have been the case for the Pleiades if these parallaxes were actually correct. The analysis included a spectral analysis of 170 G- and K- type dwarf field stars which measured accurate metallicities, temperatures, activity measures, and Lithium abundances. While not finding such subluminous objects that they were looking for, Kim et al. (2016) noted that several of the stars showed signs of youth (chromospheric emission in Balmer alpha and detectable Li absorption); however, they did not explore stellar rotation or stellar kinematics in their paper.

These indicators of youth within the field star sample pushed the question of what else can we learn from spectroscopy about the age of a singular star considering much of what is known about the ages of stars is through photometry. We intended to measure radial velocities, rotational broadening, and their errors from the raw spectra of the Kim et al. (2016) sample. The plan was for me to learn spectral analysis and reduction techniques using the IRAF[1] (Image Reduction and Analysis Facility) program from my advisor, Dr. Terndrup. However, COVID-19 postponed these plans due restrictions on building access and social distancing. This effort will be resumed during the summer of 2021. In light of this, the analysis turned to other large spectroscopic surveys in order to conduct an analysis of rotational velocities in low mass field stars and how these can be used to assign probabilistic ages to field stars using gyrochronologic models.

[1] https://iraf-community.github.io/

1.2 Gyrochronology

Stellar rotation is entangled with many mechanisms that dictate a star's formation and evolution. Much has been published on the idea of stellar angular momentum evolution. Initially, the work focused on measuring projected rotation rates ($v \sin i$) from spectral line broadening in high-resolution spectra. The advancement of calculating rotation periods from observations of periodic brightness modulations due to starspots has resulted in huge databases of rotation periods of star clusters of known age and field stars whose ages can be derived from astroseismology. From these studies and databases, it is accepted that below the Kraft Break ($1.5 M_{\odot}$), stars begin their main-sequence lives spinning relatively rapidly and spin down as they age due to the loss of angular momentum driven by the interaction of stellar winds and magnetic fields (Kraft, 1967; Skumanich, 1972). Above this mass break, stars rotate much more rapidly which is thought to be because stellar winds are less effective at altering the rotational angular momentum of the star. This is due to the shallow convective envelopes of massive stars that create weak magnetic fields.

This idea of gradual spindown for low-mass stars informs gyrochronology, the method of determining ages of stars from rotational velocity. It is typical for analyses using gyrochronology to use rotation periods rather than projected rotation rates (Mamajek & Hillenbrand, 2008; Meibom et al., 2011; Barnes, 2010); however, these rotation period detections depend highly on the activity cycle of a star, considering it uses brightness modulation from star spots to determine periods. This could lead to a bias of the distribution of rotation rates especially for older stars at the minima of their activity cycles. Considering groups of stars have a broad distribution of initial angular momenta, gyrochronological aging is poorly constrained especially for low mass stars. Using wind laws like those in Kawaler (1988) and Denissenkov et al. (2010), this broad distribution converges over timescales that increase with decreasing mass (Gallet & Bouvier, 2013; Denissenkov et al., 2010). This makes it difficult to fit a rotation-age relation for young,

low mass stars. Along with this obstacle, the use of time-series photometry is magnitude-limited and requires multiple exposures of the star over time. These selection biases will cause many dim, low-mass stars to go completely undetected and multiple exposures cost much more telescope-time and money than a single spectroscopic measurement.

1.3 Spectroscopic Rotational Velocities

A separate technique for determining the rotation rate of stars is through the broadening of stellar absorption lines in high-resolution spectra. Even if a star is at the minimum of its activity cycle, during which spots are small or absent, it will always show broadened spectral lines. While spectroscopy does not rely on variable spots on a star's surface, and can therefore detect more stars with rotation, it still has selection effects that are primarily due to detection limits and inclination angle. The inclination angle will manifest as a decrease in the detected rotation rate, thus, the distribution of rotation rates will be broadened by the distribution of inclination angles. It is appropriate to assume that this distribution is uniform, however, a uniform distribution of inclination angles averages out to $\frac{2}{\pi}$ when taking into account the $\sin i$. This will be taken into account in the analysis. More importantly, the detection limit of $v \sin i$ in our analysis is $6\,\mathrm{km\,s^{-1}}$. This means that only the rapidly rotating stars will be detected. This should not be a problem, though, as the focus of this study is on young stars and we demonstrate that stars rotating faster than the detection limit are almost certainly less than 1 Gyr.

Similar to the boom in rotation period databases, there are an abundance of large high-resolution spectroscopic studies of field stars now available due to interests in stellar abundances and kinematics or the search for exoplanets. This focus on field stars helps to make the analysis more metallicity-complete as open clusters typically have near-solar metallicities while the spectroscopic surveys contain stars of all metallicities. This will help determine if metallicity plays a role in the initial angular momentum distribution

or the way stellar winds behave. There is also evidence that there is variance in the distribution of angular momentum between different stellar clusters (Coker et al., 2016). With this in mind, there is no reason for us to suspect that stellar clusters have the same initial conditions or even the same angular momentum evolution as singular field stars. Using these spectroscopic databases with an ample amount of field stars, we can explore the interpretation of rotation rates without relying on open clusters.

2 Samples and Selection

Three spectroscopic stellar samples are used in the analysis of this paper: the sample used by Kim et al. (2016), and the catalogues presented by Buder et al. (2019) and Brewer et al. (2016). For each, Gaia DR2 astrometry and photometry were retrieved in order to derive UVW velocities and explore potential binary systems within the samples. Along with this, I use data reported by the respective papers, or data measured from the raw spectra shown in Table 1.

	$v \sin i$	RV	[Fe/H]	$T_{\rm eff}$	A(Li) or EW	$V_{\rm mag}$
Kim et al.	*	*	O	O	O	O
Brewer et al.	O	O	O	O		O
Buder et al.	O	O	O	O	O	O

Table 1: Values used in this analysis reported in the respective papers. Asterisks indicate values currently being extracted from raw spectra.

2.1 Sample Constraints

While all of the Kim et al. stars are used as the main sample for this analysis, the two additional samples are selected from such that only stars with $M_{\rm V} \geq 4.74$ and $T_{\rm eff} \leq 6000$ K are included. This is to limit the analysis to low-mass, main-sequence stars and to reduce the possibility of systematic errors due to the different evolutionary phases of the

stars turning off the main sequence at higher temperatures. Along with this, the criteria of a good parallax being $\sigma_\pi/\pi \leq 0.03$ is applied to the Gaia DR2 parallaxes of each sample. This is done to avoid large errors in parallax and/or stars lacking this data in the Gaia DR2 release. With these extra measures, there remain 331 stars and 852 stars for the Brewer and Buder samples, respectively as shown in Fig. 1 as blue markers.

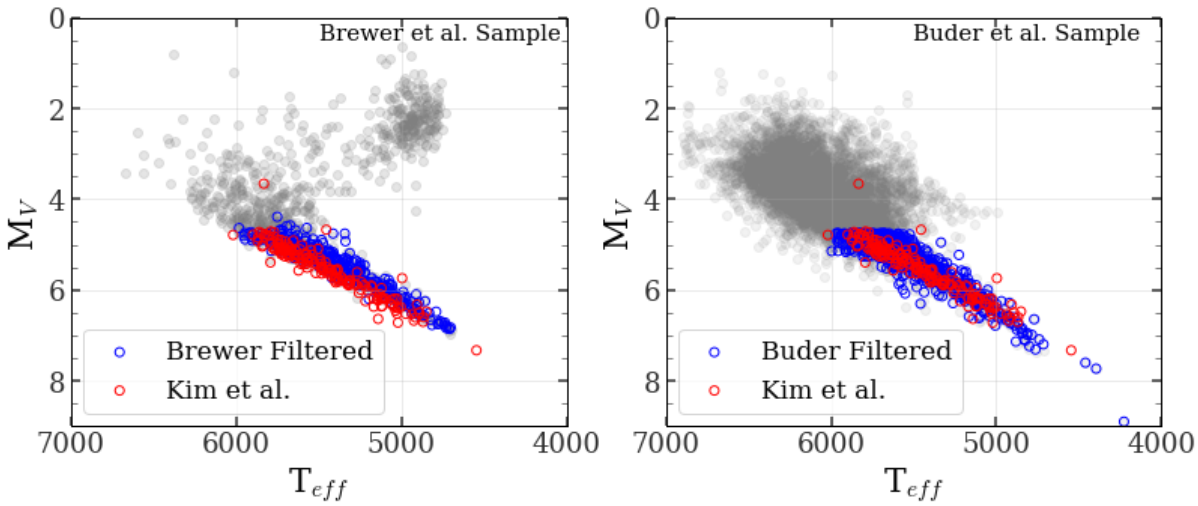

Figure 1: H-R diagram of the full Brewer et al., Buder et al., and Kim et al. samples using data reported by the respective papers. Grey markers are stars not included in this analysis and blue markers show the Brewer (left) and Buder (right) stars selected by $T_{\rm eff} < 6000$ K and $M_V > 4.74$. Red markers show the Kim sample in both panels.

2.2 Kim et al. Sample

The Kim sample is the main sample in this analysis and can be seen in both panels of Fig. 1 as red circles. This consists of 170 main-sequence field stars of spectral types G and K with 90% of the sample being within 55 parsecs (top, orange, Fig. 2). The original paper uses a color-absolute magnitude selection which includes only stars inside a parallelogram cut corresponding to $4.74 \leq M_{\rm V} \leq 6.34$ at B–$V = 0.60$ and $6.86 \leq M_{\rm V} \leq 8.46$ at B–$V = 1.0$ (Kim et al., 2016). These are all below the main sequence of the Hyades, and therefore expected to have lower metallicity than the two additional samples (center,

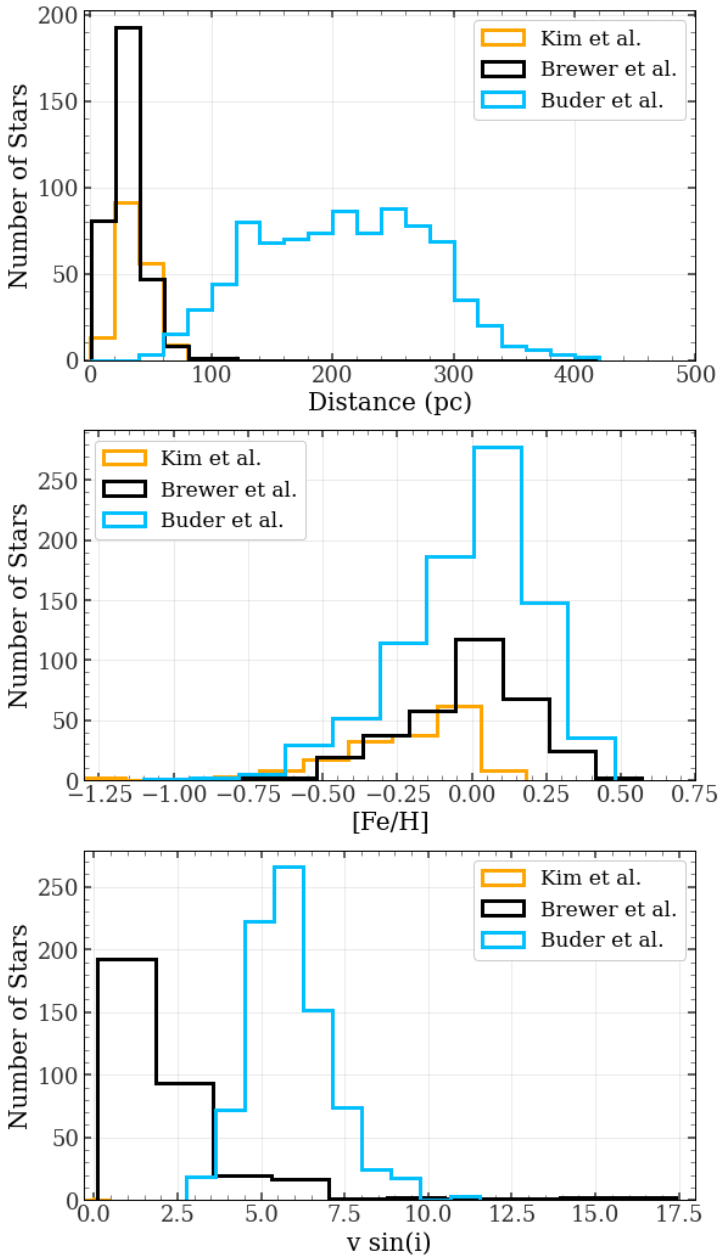

Figure 2: Distributions of distance (top), metallicity (center), and projected rotation rate (bottom) for Kim (orange), Brewer (black) and Buder (blue) samples.

orange, Fig. 2). These color cuts reduce the effects of stellar evolution for high mass stars, minimize highly convective M dwarfs which may introduce complications with Li depletion models, and decrease the possibility of binary contamination. We have obtained and are re-analyzing the high-resolution ($\lambda/\Delta\lambda \sim 60,000$) spectra for this sample.

2.3 Brewer et al. and Buder et al. Samples

The full Brewer sample contains 1,617 planet-search stars which can be seen in the right panel of Fig. 1 as the grey and blue circles. The paper makes use of the California Planet Search (CPS) which is a search for exoplanet host stars using radial velocity variations from the high-resolution spectroscopy of the HIRES spectrograph (Brewer et al., 2016). The emphasis is on bright, single stars with narrow-line spectra. This results in a selection bias against rapidly rotating stars, and therefore, a presumed bias against young stars. For the selected sub-sample explained above, these rotational velocities can be seen as the black histogram in the bottom panel of Fig. 2. Of the 331 stars in this analysis, 90% are within 55 parsecs (top, black, Fig. 2) similarly to the Kim sample. Unlike the main sample, this is not biased towards low metallicity as can be seen in the center panel of Fig. 2 with the black distribution centering on solar-metallicity values with the tails going well into the metal-rich and metal-poor domains.

The full Buder sample contains 7,066 stars in the galactic disc shown in the right panel of Fig. 1 as the grey and blue circles. The sample was initially magnitude-limited such that the apparent V magnitude calculated by the 2MASS J and K passbands is brighter than 14 mag (Buder et al., 2019, and references therein). This is limited further by neglecting binaries and stars with spectroscopic broadening velocities above 30 km/s. While there is a limit on the total spectral broadening, it is less significant than the Brewer subsample as shown by the blue distribution in the bottom panel of Fig. 2. Of the 852 stars being analyzed, 90% of them are between 60 and 300 parsecs as shown in the left panel of Fig. 2 in blue. Thus, this sample is much more distant than the two other samples and, therefore, is likely to have larger parallax uncertainties. The Buder sample remains unbiased against metallicity like the Brewer sample, shown in the center panel of Fig. 2 in blue.

In sum, the Buder sample has far more distant stars than the Kim and Brewer samples

and filters out binary stars. The Kim sample shows a more metal-poor population of stars as expected from the selection criteria of being below the Hyades main sequence. The Brewer sample selects against rapidly rotating stars, however, it has rotation rates piled up at zero calling to concern the way these measurements were assigned. Nonetheless, all samples have high-resolution spectroscopic measurements.

3 New spectra reduction

We have begun a new reduction of the spectra reported by Kim et al. (2016) to derive radial velocity and $v \sin i$, which were not reported in that paper. See the original paper for a full description of target selection and observing methods. Spectroscopy was obtained in two runs in 2010 with the echelle spectrograph on the Mayall telescope at Kitt Peak. The spectra covered 4539 – 7670 Å in 27 orders at an average sampling of 0.07 Å pixel^{-1} with a resolution of 2.2 pixels.

We began with the original, unprocessed data frames, and used IRAF for the standard calibration steps of overscan correction, bad pixel removal, cosmic-ray and field flattening. We paid particular care to the wavelength calibration and flexure correction in the determination of radial velocity. The observing routine was to obtain multiple arc spectra in the afternoons before each night, which were then averaged to bring up faint lines. Each order was fit to a 6th-degree polynomial, with the central wavelength and dispersion of each order simultaneously modeled with a 2nd degree polynomial (i.e., quadratic).

Applying this solution to all spectra on a given night produced radial velocities that were less than satisfactory. After correction for instrumental flexure using the well-resolved A and B telluric absorption bands, we found small systematic shifts in the location of telluric emission lines during the night, and measured that radial velocity differences between pairs of stars via the cross correlation depended systematically on wavelength. We attributed this to temperature changes in the spectrograph during each night. We

therefore introduced a time-dependent term in the wavelength solution and, as discussed below, were able to derive radial velocities to a precision of about 0.3 km s^{-1}. This is about a factor of 3 improvement over the accuracy without the extra time-dependent correction to the wavelength solution.

4 Binarity

Frequently, stellar samples used to explore wind laws and other theories of rotational evolution make no note of the binary systems within them (Keppens et al., 1995; Denissenkov et al., 2010). This is an important aspect to look into especially for solar-like stars, as roughly half of these stars are in binary systems or at least have companions (Raghavan et al., 2010; Moe & Di Stefano, 2017). This is a problem because we know there are potentially large effects of binarity, notably the effect of synchronized binary systems on spin-down and gyrochronology (Angus et al., 2020) and on rotational velocity measurement errors due to SB1 spectra being analyzed as single star spectra (Simonian et al., 2020). The angular momentum of tidally locked systems is, in large part, stored in the orbit. Therefore, the system's angular momentum loss largely comes from its orbit rather than from the rotation. Thus, binary systems may maintain rapid rotation for a much longer timescale than for single stars.

Simonian et al. (2019) calculated the photometric luminosity excesses of two samples of stars from McQuillan et al. (2014) and APOGEE. The results show that the sample of stars that are rapidly rotating ($1.5 \leq P \leq 7$ days) contains a significantly higher fraction of stars with luminosity excess than those with longer periods; thus, short-period stars are often photometric binaries. The paper suggests that the domain of rapidly rotating stars is dominated by tidally synchronized binaries. This idea could be further analyzed by comparing the spectroscopic time-domain radial velocity curve (that which designates the orbital period of the system) to the photometric rotation period due to star spot

modulation. If the two periods are uniform, the system is tidally locked. This analysis has been postponed due to COVID-19 restrictions on telescope observations, but the results above demonstrate that there will likely be a large subsample of binary systems that skew rapid rotator data.

While Brewer et al. doesn't filter out the binary systems from their sample, they do identify 16 binary stars in the full sample and distinguish between single and binary stars in their analysis. The SIMBAD Astronomoical database has identified 17 spectroscopic binaries and 4 RS CVn-type variables in the selected sample for this paper. Buder et al. has already eliminated double-lined spectroscopic and photometric binaries from their sample of which they found 448 and 338, respectively in the full sample. No additional candidates were found in the SIMBAD system for the sample used in this paper. Kim et al. identified 7 binary systems within the sample using the 9th catalog of spectroscopic binary orbits (Pourbaix et al., 2004) and 12 spectroscopic binaries were found through SIMBAD within this sample. I use two methods, radial velocity variations and photometric excess, to identify the known binaries in the samples as well as detect new systems that have since gone unnoticed.

4.1 Radial Velocity Variations

If the stars in these samples are indeed singular, the radial velocities captured during each epoch should simply be due to their motions in space; therefore constant in time with slight variation due to uncertainties. If the stars have companions, the radial velocities are due to their motion through space plus the orbit of the star around the system's barycenter. At different phases within the orbit (i.e. different epochs of data), the measured velocity will differ due to this change in motion. A significant difference in radial velocity that would trigger deeper analysis into binarity is that which exceeds 3σ above or below zero after correcting for zero-point offsets between data sets due to systematic errors (Table 2).

Sample	Kim	Brewer	Buder
Z-P Offset (Gaia)	-0.418	0.564	-0.275
Z-P Offset (Standards)	0.014	0.478	-

Table 2: First row: Zero-point offset of the ($RV_{Gaia} - RV_{sample}$) values used to find binarity. Second row: Z-P offset of the ($RV_{RVS} - RV_{sample}$) value used to calculate uncertainties in the sample radial velocities.

For each sample, I have at least two epochs of radial velocity measurements for over 90% of the stars. The Buder and Brewer samples have radial velocity measurements from their original data and Gaia DR2 (van Leeuwen et al., 2018). The Kim sample spectra are being reduced currently with 31 radial velocities extracted, of which all are also in Gaia DR2. The Kim and Brewer stars also have overlap with the Gaia DR2 catalogue of radial velocity standard stars (Soubiran et al., 2018), RVS, which is used to define errors for the reported radial velocities.

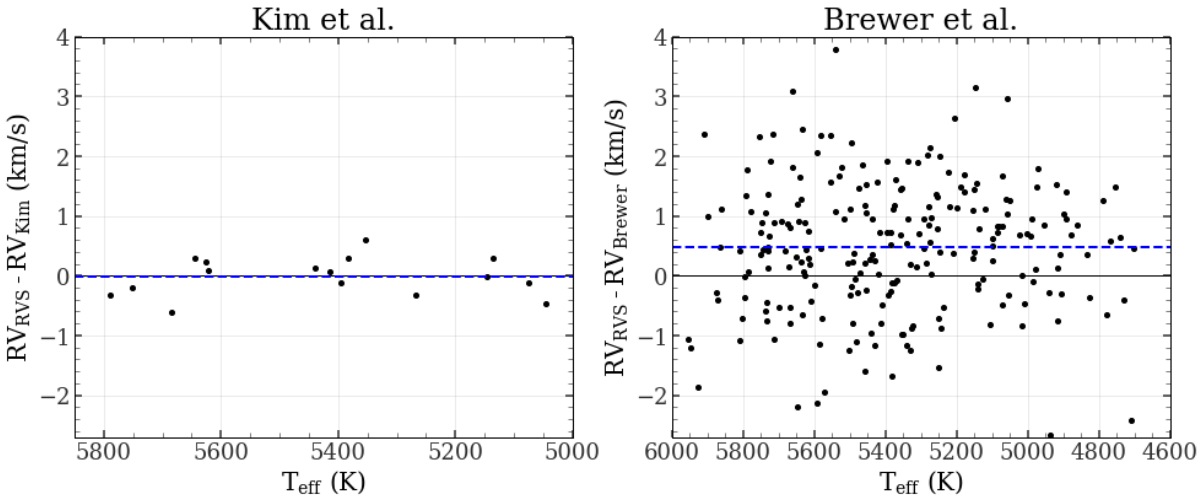

Figure 3: Radial velocity differences of stars in the Kim (left) and Brewer (right) samples that overlap with the RVS catalogue. The blue dashed line shows the average of the differences used as the Z-P offset.

Of the 170 stars in the Kim sample, there are 96 stars in common with the RVS catalogue. Of the 31 radial velocities measured thus far, 16 are in common. By finding the spread in the differences between the measured and standard radial velocities, I deter-

mine the uncertainties in the radial velocity measurements from our spectral reduction (Fig. 3). The adopted uncertainty of for these radial velocities is $0.31\,\mathrm{km\,s^{-1}}$. As Brewer et al. (2016) did not report radial velocity errors, this same method is used for the 226 stable stars overlapping between the RVS catalog and Brewer sample. After systematic corrections (Table 2), this resulted in a $1.08\,\mathrm{km\,s^{-1}}$ uncertainty. This process was not used for the Buder sample as they reported the original errors and only had one star in common with the RVS catalog.

Radial velocity variability requires both small orbital separations and orbital inclination angles much larger than zero to detect a possible binary system; therefore, not all systems are detectable with this method. For example, a system of solar-like, equal-mass stars with a semi-major axis of 1 AU and an inclination angle of 90 degrees will have a maximum radial velocity of about 45 km $\mathrm{s^{-1}}$.

The absolute value of the difference between Gaia DR2 radial velocities and sample radial velocities is found after correcting for the systematic zero-point offsets tabulated in Table 2. Using the uncertainty values described above, the error for the difference is simply the quadrature sum of the two radial velocity errors:

$$\sigma^2 = \sigma^2_{\mathrm{Gaia}} + \sigma^2_{\mathrm{adopted}}. \tag{1}$$

Using this uncertainty, if any difference satisfies $|\mathrm{RV_{RVS}} - \mathrm{RV_x}| \geq 3\sigma$, it is further analyzed to determine binarity. These corrected differences and their errors are shown in Fig. 4.

Through this, no candidates demonstrating radial velocity variations out of 31 stars were found in the Kim sample; however, the one apparent point less than 5000 K in Fig. 4 is flagged as a possible spectroscopic binary despite the cutoff. 20 spectroscopic binary candidates were found out of 318 stars with Gaia DR2 radial velocities in the Brewer sample, and 44 out of 805 stars with Gaia DR2 radial velocities in the Buder sample. This results in a 3%, 6%, and 5% spectroscopic binary population in the Kim,

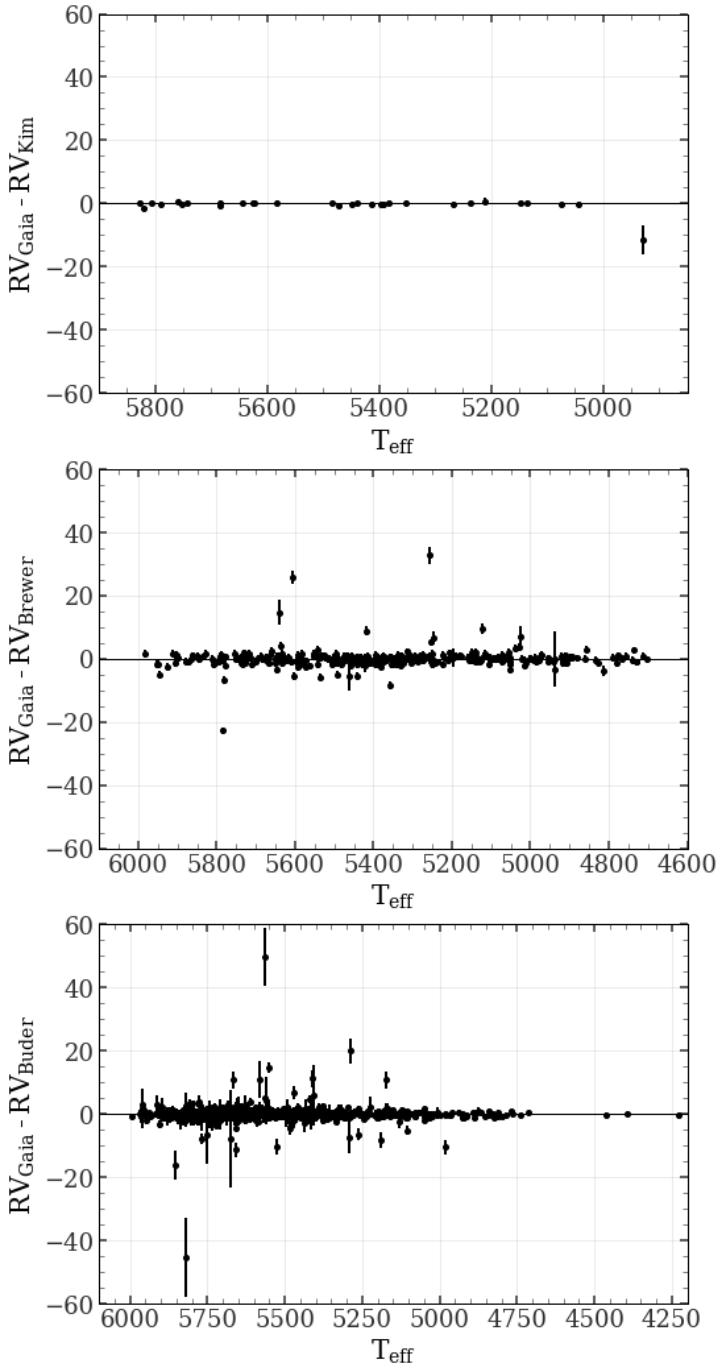

Figure 4: Radial velocity differences of Gaia radial velocities minus the ground based measurements for the full samples with error bars showing the propagated errors of the difference. Any difference three times these errors are considered binary candidates.

Brewer, and Buder samples respectively. Though the Kim sample is lacking too many measurements for this to confidently represent the true value, the lack of binary systems is promising considering the selection criteria. Once the spectra are fully reduced for this sample, a more accurate population of possible spectroscopic binaries may be claimed.

The unexpected binaries in the Buder sample may be due to an underestimation of the errors or actual binary infiltration into the sample considering 5% is a significant fraction outside of the 3σ range.

4.2 Photometric Excess

If a binary star system is unresolved during the time of photometric exposure, the light from the two stars combined will be interpreted as light from one star. This means that at a given color or temperature, the star will appear brighter (i.e. slightly above the main sequence). For an equal mass binary, one in which both components are the same size, double the light will be detected, thus double the luminosity. Considering the equation for apparent magnitude given luminosity is

$$m_1 = m_2 - 2.5 \log \left(\frac{L_1}{L_2} \right), \tag{2}$$

the expected magnitude difference for equal mass binaries would not be two times the magnitude due to the logarithmic relationship on luminosity. Rather, the expected gap would be

$$\delta M = m_{\text{binary}} - m_{\text{single}} = 2.5 \log \left(\frac{L_1}{2 \cdot L_1} \right) = -0.75. \tag{3}$$

Following this logic, systems with three unresolved equal mass stars would have a discrepancy of -1.2. Thus, to find stars with sizable companions, we look for stars that are brighter than the main sequence by up to ~ 1.2 magnitudes. Note that not all systems

have equal mass ratios and therefore will have smaller discrepancies from the single-star main sequence.

Because giants and subgiants also reside above the main sequence, it is evident that it is necessary to only analyze unevolved main-sequence stars in order to avoid the effects of the evolutionary phase on stellar luminosity. In the domain that the samples of this analysis are selected (excluding the high-mass end of the Buder sample), the stars have low enough masses that main-sequence turnoff should not be an issue. See section 2.1 for a discussion on selection criteria.

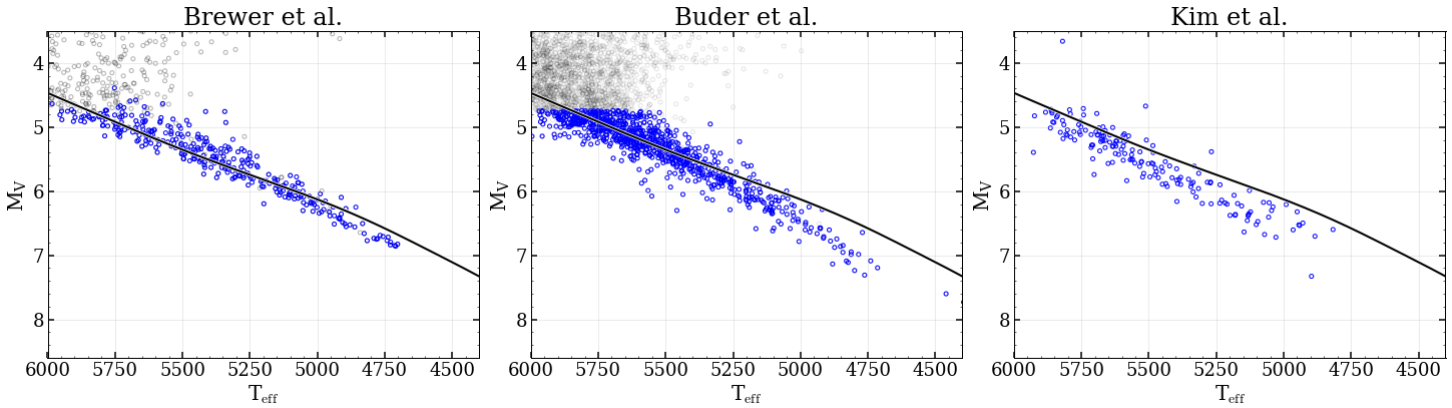

Figure 5: H-R diagram as in figure 1 with the plotting window zoomed in to the main sequence and an empirical Hyades isochrone from Pinsonneault et al. (2004) to show the difference in temperature determinations.

To quantitatively see the magnitude excess of the stars on the main sequence, the detrending of the main sequence is required. As can be seen by plotting an empirical isochrone for the Hyades in absolute V magnitude and effective temperature from Pinsonneault et al. (2004) in Fig. 5, Buder et al. has adopted temperature values about 200 degrees hotter than Brewer et al. in their spectroscopic analysis below 5000 K. This emphasizes the necessity of careful spectral reduction and attention to uncertainties. Due to a lack of overlap between these two samples, this cannot be analyzed further here.

Instead of using the values adopted from the respective papers, we use photometric data from Gaia DR2 shown in the top panels of Fig. 6 in order to avoid any systematics.

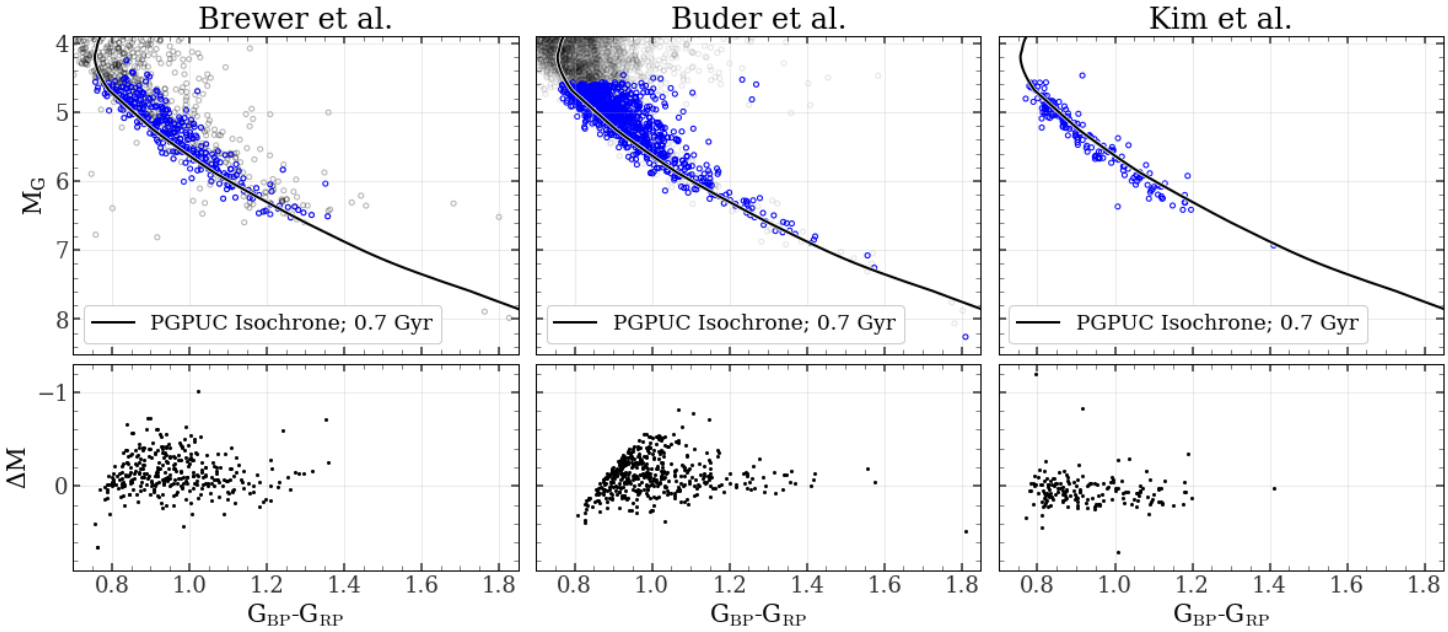

Figure 6: Top: Color-magnitude diagram. Blue markers indicate samples used in this analysis with a Princeton-Goddard isochrone[2] overlaid. Bottom: Color detrended magnitudes where $\Delta \mathrm{M} = \mathrm{M_G} - \mathrm{M_G}(\mathrm{Isochrone})$.

By changing the plotted values from M_V-$T_{\rm eff}$ to $M_G - (BP - RP)$, three obvious subgiants become evident in the Buder sample as well as a population of unwanted evolved stars. To keep these out of the analysis, another magnitude cut of $M_G \geq 5$ is applied only to the Buder sample for this photometric analysis. This figure also includes an isochrone of the same color-magnitude relation calculated using the Princeton-Goddard-PUC (PGPUC) evolutionary code[2]. This isochrone is linearly interpolated in order to subtract it from the given absolute magnitudes of each sample. This detrends the main sequence in relation to color.

The vertical displacements of the magnitudes in reference to the PGPUC isochrone ($\Delta M = M_G - M_G(\text{PGPUC Isochrone})$) are shown in the bottom panels of Fig. 6. As expected, the majority of the Kim sample falls below the isochrone because the Kim sample was originally selected to reside below the Hyades main sequence to explore subluminous

[2] The Princeton-Godard PUC evolutionary code may be accessed at the "PGPUC Online" website (http://www2.astro.puc.cl/pgpuc/iso.php). This isochone has Z = 0.024 Y = 0.26 [α/Fe] = 0.00 η = 0.00 t(Gyr) = 0.7.

stars. There also appears to be structure in the Brewer and Buder samples at bluer color indexes, but this is artificial due to the magnitude cuts discussed in section 2.1.

Before searching for multiple systems within these samples, the effect of metallicity on the main sequence must be detrended as well. This is especially important as we are adopting metallicities from three different studies which we have already seen assign different values for effective temperature. This will affect the spectroscopically determined [Fe/H] values where Buder may have lower [Fe/H] for their hotter temperature adoptions. Lower metallicity stars appear to be bluer than their mid- to high- metallicity counterparts. This manifests in metal-rich stars appearing to be more luminous on a color-magnitude diagram for a given color. This will not only broaden the main sequence of single stars, but also will create problems in finding the binary sequence above the main sequence.

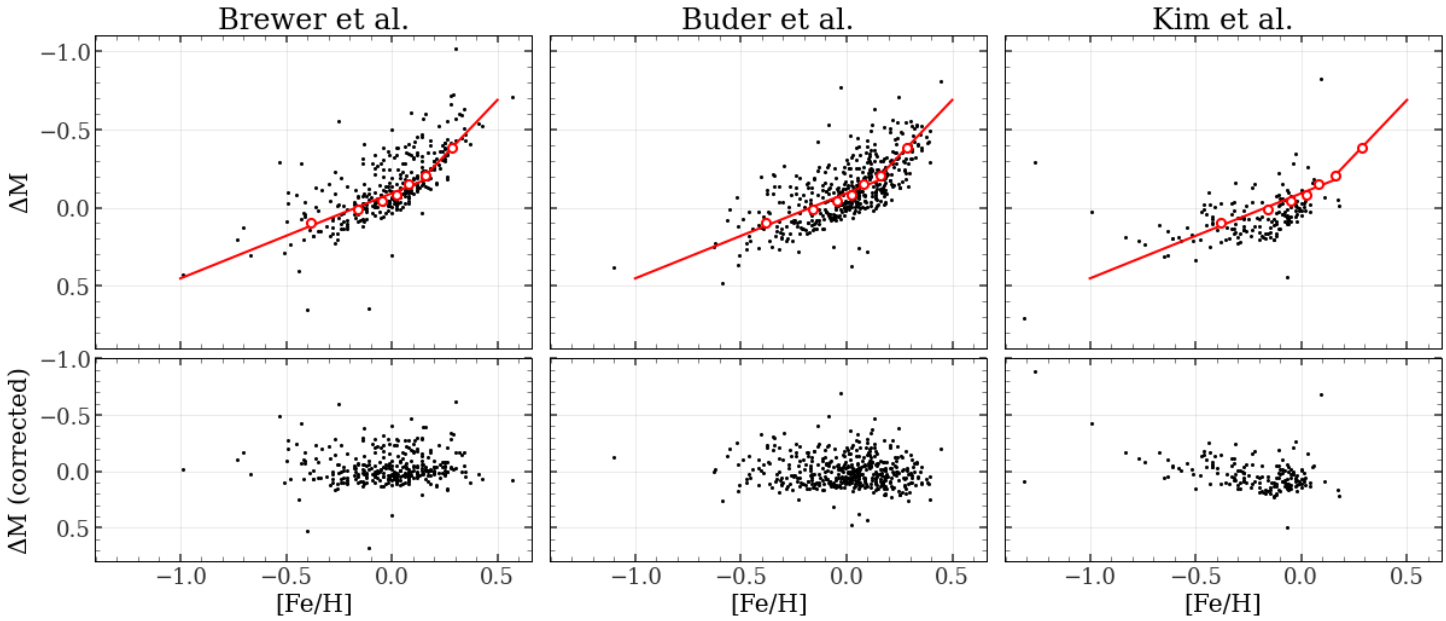

Figure 7: Top: ΔM from Fig. 6 against metallicity with two linear fits plotted in red to the equally binned values of the combined Brewer and Buder data. Bottom: Corrected ΔM by subtracting the model in red from the original ΔM.

As can be seen in Fig. 7, there are trends in the color-detrended main sequence against

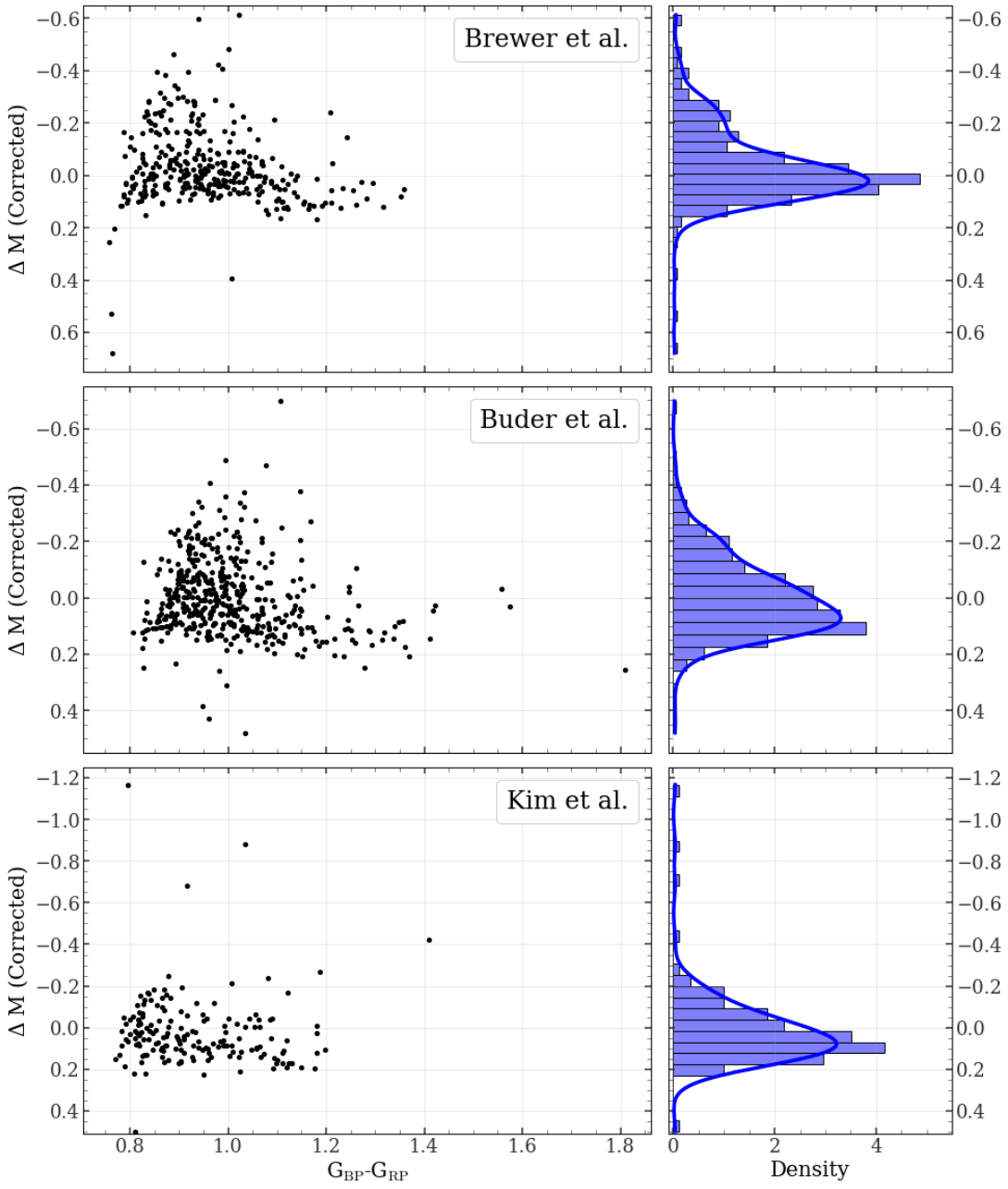

Figure 8: The metallicity-corrected ΔM from Fig. 7 against color for each sample with a kernal density estimation shown in the right.

[Fe/H] that follow the expected magnitude-metallicity trends. To model this data, I combine the Buder and Brewer samples in order to have a metallicity-complete sample. I then find the 50th percentile of 7 equally-populated metallicity bins. This is to ensure the magnitude excess of the binary sequence would not be taken into account in the model

fit. The average metallicity of each bin is used in order to create characterizing points in the ΔM - [Fe/H] plane. These seven percentiles are plotted in the top panels of Fig. 7 as red unfilled circles. A piece-wise function of two linear models are fit to the binned percentiles for the combined sample of Buder and Bruder and is shown as the red line in the same figure. This model is then subtracted from all three isochrone-detrended samples to detrend the data with respect to metallicity. The residuals are shown in the bottom panels of Fig. 7.

Returning to the color-magnitude plane, the color- and metallicity-detrended main sequence is shown in the left columns of Fig. 8. The right column shows the distributions of ΔM(Corrected) for each sample. From the overlaid kernel density estimates, it is evident that there is a population of stars with a magnitude excesses of $\Delta M \leq -0.15$ in the Brewer and Buder samples. This is less obvious in the Kim sample from the kernel density function as we do not expect photometric binaries, however, obvious outliers indicate binarity below -0.3.

Kim Sample		Brewer Sample		Buder Sample	
HIP	ΔM	HD	ΔM	Gaia Source ID	ΔM
1674	-0.24	10145	-0.32	4688315489190138624	-0.38
14241	-0.25	10700	-0.48	63408977309516800	-0.36
23786	-0.22	168746	-0.39	39517311193365120	-0.34
63322	-0.27	210277	-0.39	49785199310934784	-0.41
83276	-1.18	4741	-0.41	65452866348200320	-0.32
97640	-0.88	10790	-0.61	*4676760893292184192	-0.31
99965	-0.68	19617	-0.39	5199874509648979840	-0.38
106231	-0.42	*61994	-0.46	6301939680162772992	-0.34
		112415	-0.34	6270589786156487296	-0.30
		161198	-0.42	6246952489482132736	-0.70
		*161479	-0.33	6362883719904615680	-0.47
		*190412	-0.60	*4220355021056217984	-0.49
				6357025560608129664	-0.32

Table 3: Photometric binary candidates as determined by metallicity-corrected magnitude excesses in each sample. Asterisks show stars which are also spectroscopic binary candidates.

When searched in SIMBAD, the Brewer sample contained 4 known RS CVn-type variables but no other photometric binaries (see section 4 for spectroscopic binary discussion). The Buder sample contained no known photometric binaries in SIMBAD. As the Kim sample is selected to be subluminous, it is likely that there should be no photometric binaries despite what would be expected by Simonian et al. (2019) due to the presence of rapid rotators in the sample, but it still only contained possible spectroscopic binaries.

Applying a moderate cut of $\Delta M(\text{Corrected}) = -0.3$ to the Buder and Brewer samples and -0.2 to the Kim sample, I recovered some of the stars that are flagged as spectroscopic binaries by SIMBAD and several undiscovered photometric binary candidates. The stars that have vertical displacements above the main sequence enough to make them photometric binary candidates are shown in Table 3 of which 8 are in the 170 Kim stars, 12 are from the 331 Brewer stars, and 13 are in the 852 Buder stars. This shows a photometric binary population of about 5%, 4%, and 2% for the Kim, Brewer, and Buder samples respectively.

5 Youth Indicators

There are three characteristics of stars that I focus on in this project that are indicators of youth. These include rapid rotation, which is discussed in the next section, detectable lithium abundance, and cool galactic kinematics. A fourth spectroscopically available indicator is stellar activity, which may be analyzed in later papers using the R'_{HK} activity indicator.

The kinematics of a population of stars is a rough estimate of stellar age because stars form kinematically cold, meaning they have relatively low velocity dispersions in the U, V, and W velocities (Almeida-Fernandes & Rocha-Pinto, 2018). This can be seen in the younger Population I stars that reside in the galactic disk and follow a normal, mostly-circular orbit (Grieves et al., 2018). As stars age, dynamical heating results in an increase

of velocity dispersion, namely in the W direction (Mackereth et al., 2019), so a sample of stars with a small velocity dispersion is expected to have a young age as can be seen in Fig. 9 and Fig. 10 later in this discussion. The U, V, and W velocities of each sample were calculated using the method put forth by Johnson & Soderblom (1987). Parallaxes, proper motions, and radial velocities retrieved from Gaia DR2 were used to derive the kinematics of each sample.

Lithium abundance indicates youth due to the fragility of lithium in stellar interiors. It is easily destroyed by proton capture at temperatures near and above 2.5 million Kelvin (Pinsonneault, 1997). Lithium in the photosphere of the star migrates to the stellar interior through convective zones at a timescale less than the stellar lifetime, so if a star has a significant lithium abundance measured through spectra, it is evident that it is likely to be a young star (Burke et al., 2004). This is especially evident at the lower masses of these samples due to the large convective envelopes in low-mass stars leading to a higher possibility of lithium migrating to the stellar interior.

Lithium abundance is reported in the spectroscopic analysis of the original Kim and Buder papers. In the Kim et al. (2016) analysis, the equivalent widths of the lithium absorption line at 6707.70 Å were measured. The original paper took an equivalent width of about 50 mÅ to be considered a "high" lithium youth indicator. In this analysis, any star having an EW higher than the average value of the detectable lithium sample, 46.5, is considered to have a "high" lithium abundance. In the Buder et al. (2019) analysis, the absolute lithium abundance of the stars were measured using 1D non-LTE corrections to the spectra. The average value of this measure for the full Buder sample, 1.5, is used in this analysis to designate "high" lithium abundance.

To determine if the youth indicators extracted from spectra (lithium and rotation) are sufficient in determining youth, I compare the kinematics of the population of young candidates to the rest of the sample. These comparisons can be seen in Fig. 9 and Fig. 10 where high-lithium means greater than the average lithium abundance of the respective

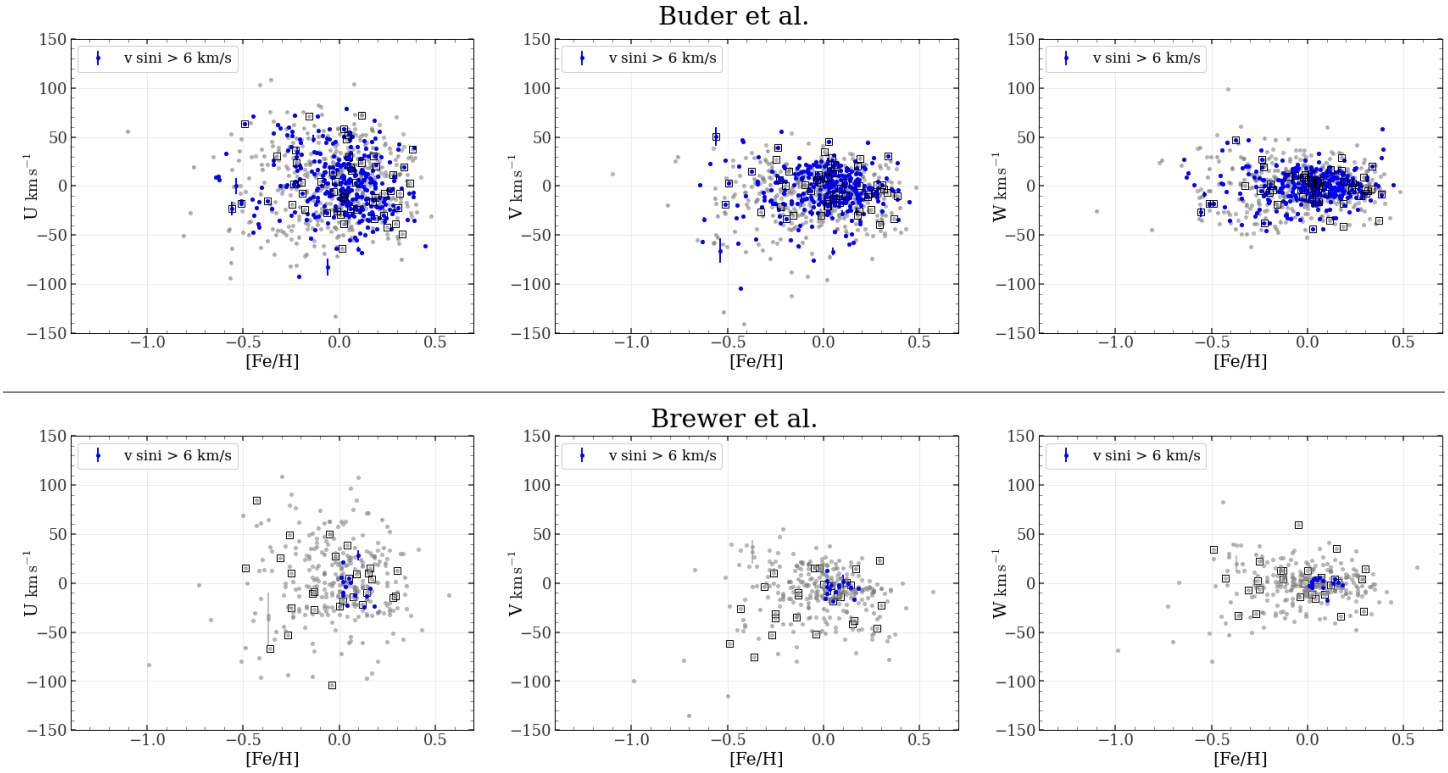

Figure 9: Stellar kinematics of each sample with blue markers indicating rapid rotation ($\geq 6\,\mathrm{km\,s^{-1}}$) and therefore possible young stars. Markers with black squares around them designate photometric and spectroscopic binary candidates as found in section 4.

samples and rapidly rotating means having a rotation rate greater than $6\,\mathrm{km\,s^{-1}}$. As can be seen from this data, and in agreement with other studies (Wu et al., 2021; Spagna et al., 2010; Bovy et al., 2012, and references therein), rapid rotation and high lithium content coexist with cool kinematics, especially in the W direction: all pointing to a young population.

The velocity dispersion for each direction and population are found by finding the standard deviation of the velocities. These can be found in Table 4. As can be seen, the velocity dispersions for the full samples are larger than the candidate young population. While the difference between young and old kinematics is stark in the Kim and Brewer samples, it is not as drastic in the Buder sample. This is probably due to the small number of young candidates in the Kim and Brewer samples, especially considering the

Brewer sample is biased towards narrow-lined spectra (slow rotation).

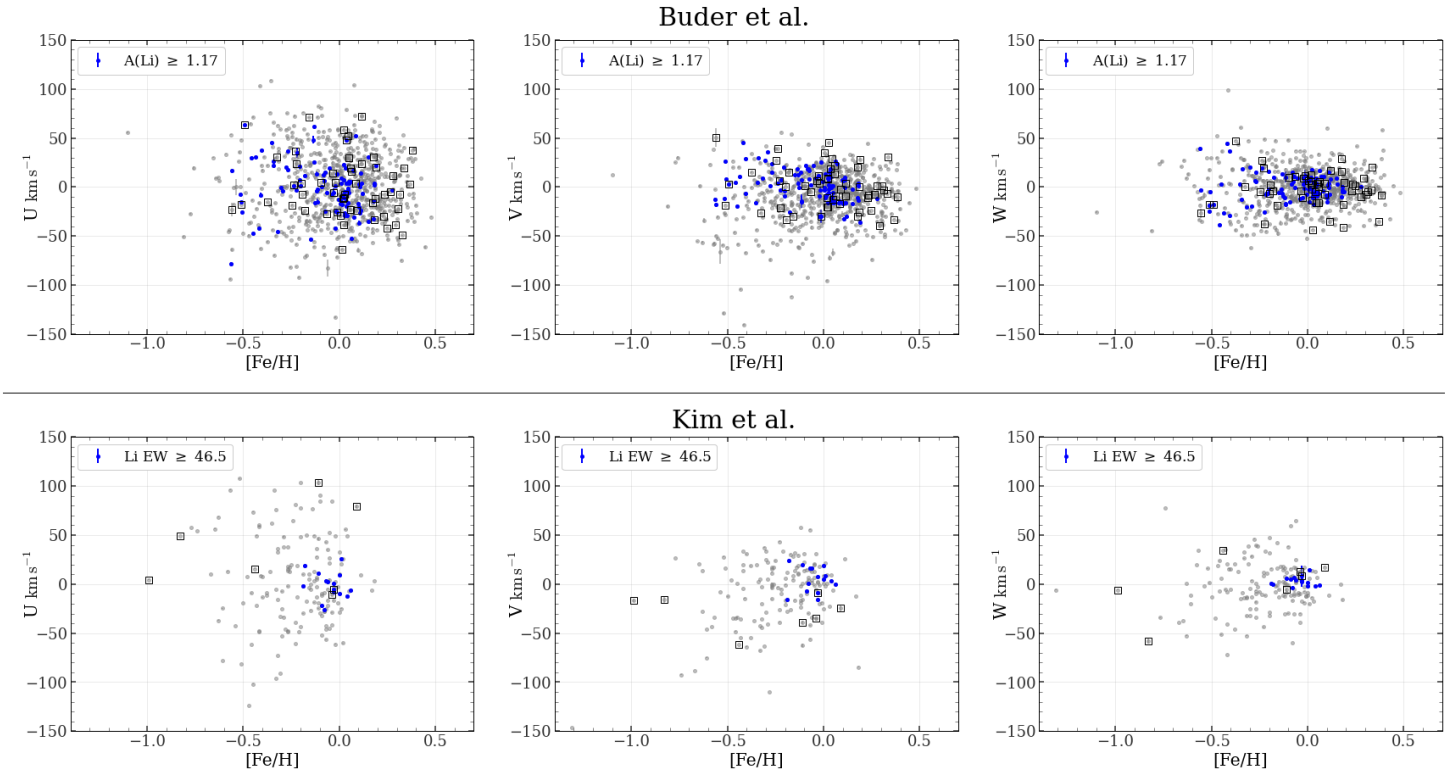

Figure 10: Same as figure 10, but with blue markers indicating high lithium abundance.

	Kim			Brewer			Buder		
$(\mathrm{km\,s^{-1}}) \rightarrow$	σ_U	σ_V	σ_W	σ_U	σ_V	σ_W	σ_U	σ_V	σ_W
Full Sample	51.1	32.2	24.8	38.1	26.3	19.1	36.0	25.8	20.3
Rapid Rotator	-	-	-	14.5	7.7	5.4	29.3	21.3	15.7
Lithium-Rich	13.5	12.4	4.5	-	-	-	25.6	16.1	13.7

Table 4: Velocity dispersions in each of the U, V, and W velocity directions for the populations of candidate young stars based on rapid rotation and high lithium content and the stars outside of this population.

However, the much more complete Buder sample, as can be seen by the large number of blue markers in Fig. 9 and Fig. 10, still supports cool kinematics for the lithium-rich and rapid rotation populations. This is a promising result hinting that rotation and lithium work in similar ways. The lithium-rich population in the Buder paper having even cooler

kinematics than the rapid rotators gives evidence that lithium depletion works at time scales shorter than the typical spin-down of low-mass stars. With further support for rotation and lithium content working in similar ways, we can use this to better constrain the ages of stars not only based on gyrochronology but also by including lithium content into our analysis.

6 Ages and Projected Rotation Rates

6.1 Angular momentum evolution models

The initial angular momentum evolution model in this analysis is adopted from Denissenkov et al. (2010). Treating open clusters as an evolutionary sequence, this paper statistically compared observed rotational period distributions of aged open clusters to three types of evolutionary models. These include a double-zone model in which the core and outer envelope rotate as separate solid bodies, and two full stellar evolution models. Settling on the double-zone model, Fig. 11 shows the period-age plane with evolutionary models plotted on the observed open cluster data for solar-like stars.

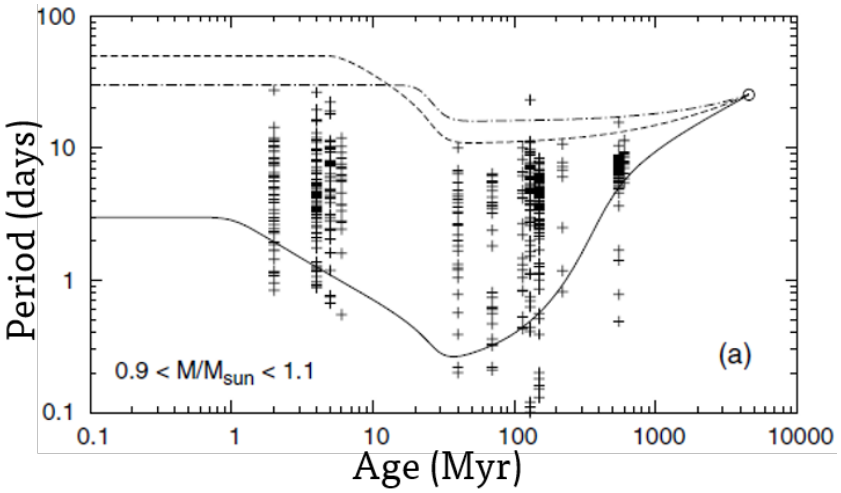

Figure 11: Rotation period data (plusses) of solar-like stars in clusters versus age from Denissenkov et al. (2010). Curves show the study's evolutionary model. The solid curve depicts a typical initial period and the dashed curves show those longer than observed.

Using an initial period distribution calculated using the youngest open clusters in their data, it is found that a double-zone model with observationally constrained disk-locking and core-envelope (τ_c) coupling timescales works to evolve this distribution to match those of older open clusters for the fastest rotating stars in the distribution. However, the reasonable value of $\tau_c = 1$ Myr used for the rapid rotators does not produce the slowly rotating population of stars until the coupling timescale increases to over 50 Myr up to 300 Myr depending on mass. This demonstrates that the double-zone model will not work if all stars are assumed to follow solid body rotation. Considering the emphasis of this analysis on rapid rotation in young stars, this technicality in the slow-rotator models should not pose any complications.

Even in clusters with a well defined age based on the main-sequence turnoff, there is a wide range of periods and therefore a wide range of rotation rates at a given age. It is known that, for stars below one solar mass, there is a broad range of rotation rates on the zero-age main sequence. By nearly 600 Myr these values converge due to the fact that angular momentum loss depends on rotation rate and that the models are constrained to solar values at 4.6 Gyr. This is shown in Fig. 11 as the rotation rate distribution of the Hyades at age 600 Myr has drastically narrowed excluding some outlying rapid rotators.

This is helpful for mid-mass G stars, but as mass decreases further, the convergence time increases leaving large distributions of rotation even at older ages for low mass stars. Due to this, the current analysis produces probabilistic upper limits on the ages of these low-mass stars. For example, the detection limit of rotational velocity from the spectra in the Kim sample is about 6 $\mathrm{km\,s^{-1}}$. For a solar-like star, this limit corresponds to a period of about 7 days which, in turn, corresponds to an upper age limit of about 600 Myr that can bee seen in the fast-rotating (solid line) in Fig. 11. This means any stars with detectable rotation rates in our spectra (that is, over $6\,\mathrm{km\,s^{-1}}$) will have a high certainty of being young stars or at least younger than the Hyades cluster.

6.2 Age Assignments

Using the simple differentially-rotating, double-zone evolutionary model described above, we have populated a theoretical distribution of $v \sin i$ versus age with a randomly distributed assignment of inclination angle. This is shown in Fig. 12 where the dashed line is at the detection limit of our main sample. As mentioned above, due to the upper envelope in the rotation rate-age distribution, a measurement above the detection limit is evidence of stellar youth. An unresolved $v \sin i$ does not necessarily indicate an old star because stars may hit the zero-age main-sequence with both large and small angular momenta and the inclination angle may skew the rotation rate lower than it actually is. The convergence of the rotation values at older ages aids in assigning upper limits in age.

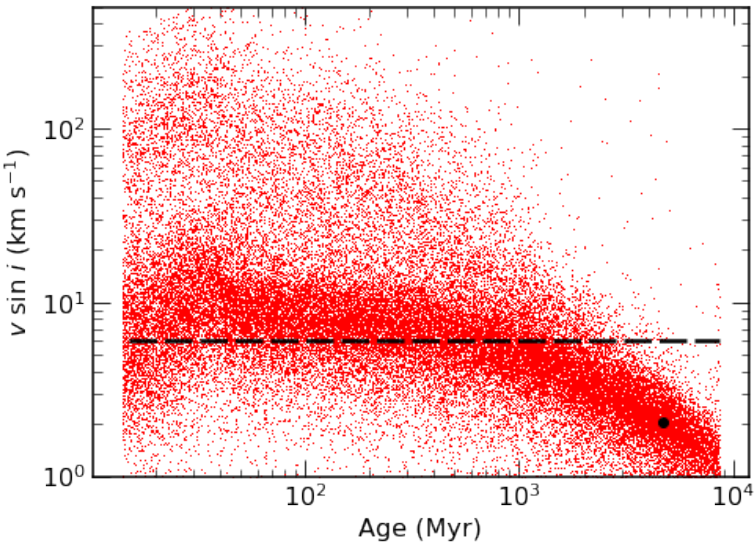

Figure 12: Theoretical distribution of projected rotation at each stellar age based on the Denissenkov et al. (2010) models for solar-like stars with a random distribution of inclination angles. The dashed line identifies the detection limit of 6 km s^{-1} and the black point shows solar values.

These upper limits are necessarily probabilistic for two reasons. First, since so many ages can correspond to one rotation measurement, it is evident that these will be probabilistic in nature. Second, the posterior on age gets broadened further due to the incli-

nation angle in our rotation measurements. The $\sin i$ part of the rotational measurement blurs the true rotation distribution further than the actual distribution.

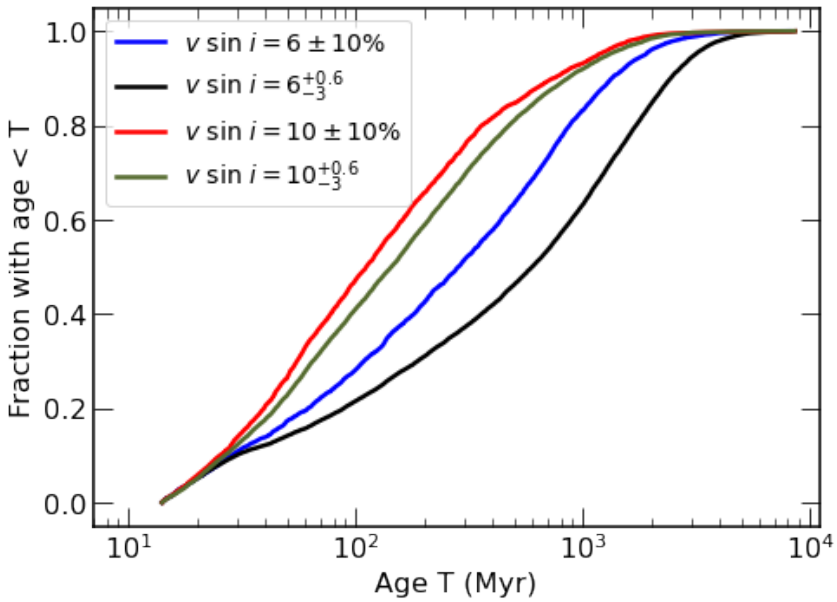

Figure 13: Theoretical cumulative age distribution for stars at the detection limit (blue & black) and above the detection limit (red & green) with Gaussian errors and errors derived from preliminary experiments on measureing $v \sin i$ in the Kim et al. (2016) spectra.

Along with these effects, the contribution of the uncertainties in $v \sin i$ to the derived ages is sufficiently small unless it is near the detection limit. Fig. 13 shows the effects of the uncertainties in the projected rotational velocity where the blue and red curves show typical Gaussian errors assigned to values of $v \sin i$ and the black and green lines show errors typical of analyses that use careful probabilistic modeling to find the rotational velocities. While in both cases the Gaussian uncertainties predict a younger upper limit on age than the careful probabilistic errors, it is evident that these differences do not create huge disparities when the rotational velocity measurement is not near the detection limit. There is a much larger age difference for the 90th percentile of the 6 $\mathrm{km\,s^{-1}}$ curves than the 10 $\mathrm{km\,s^{-1}}$ curves.

Taking a horizontal cut of Fig. 12 at various rotation rates with a width corresponding

to its error will return a distribution of ages for that rotation rate. Compiled into a cumulative distribution, these cuts can be seen in Fig. 14. This provides evidence that stars with a detectable rotation rate are almost certainly less than 1 Gyr. For stars rotating faster than the detection limit, this upper limit of 1 Gyr is even more certain as shown by the green (top) curve denoting a rotation rate of 16 $\mathrm{km\,s^{-1}}$ in Fig. 14.

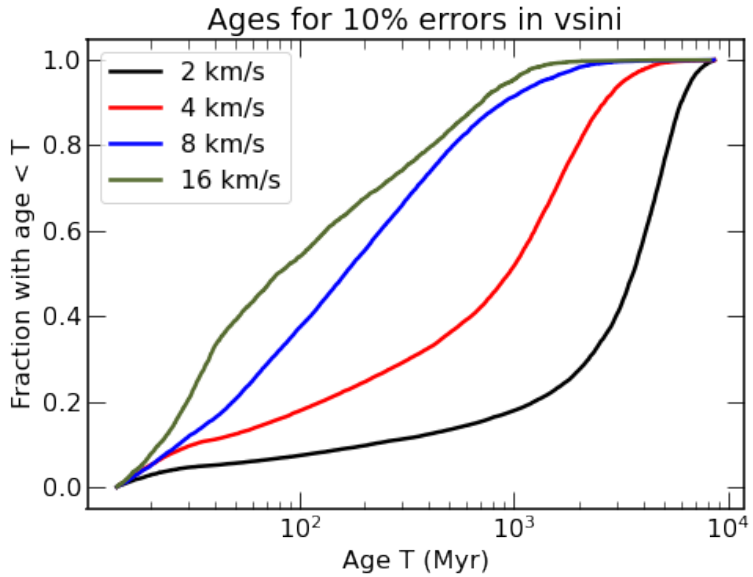

Figure 14: Theoretical cumulative distribution for ages of stars with projected rotation rates of 2, 4, 6, and 16 $\mathrm{km\,s^{-1}}$ showing that any resolved rotation in this analysis will denote a young star.

Using to our advantage the upper envelope where there is a dearth of rapid rotators at old ages, we can determine the upper 90th percentile of rotation bins in order to assign upper limits on the age of a star given a specific rotation rate. Visually, this would be done by finding the age at which a horizontal line drawn at $y = 0.9$ intersects with the cumulative distribution curves in Fig. 14. These values can be seen in Fig. 15. It is evident from these models that, with 90% confidence, we will be able to assign an upper limit to the age of a star given one careful measurement of a projected rotation rate from its spectrum. As expected, stars with rotation rates above our detection limit have upper limits that still remain young.

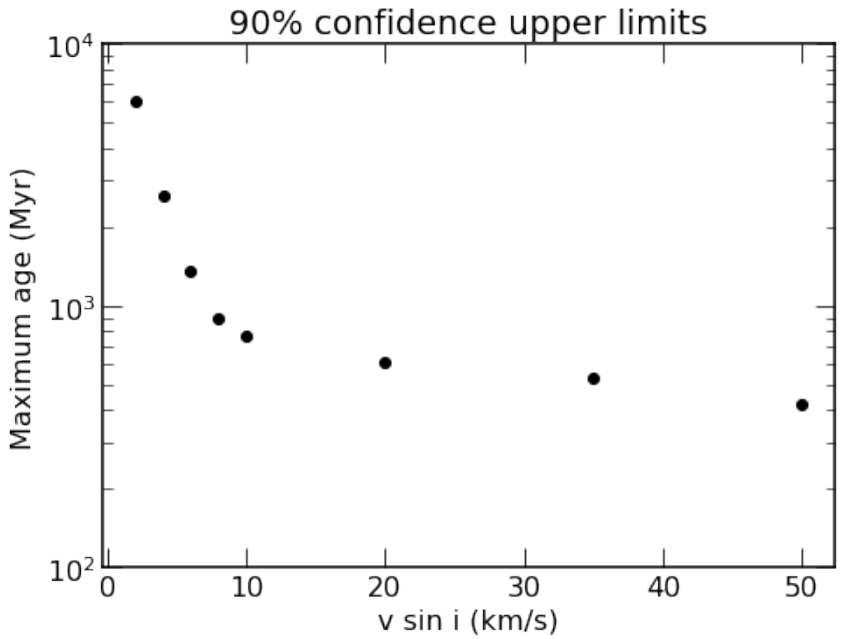

Figure 15: The 90% confidence upper limits on age for stars with various projected rotation rates.

7 Conclusions and Future Efforts

In this analysis, we synthesize data from three statistically different spectroscopic samples to determine ages from rotation rates, lithium content, and stellar kinematics while taking into consideration the binary populations in each sample. From this, we have concluded:

- The population of either spectroscopic or photometric binaries is only about 5% in each sample despite the selection biases. This seems at variance with the findings of Simonian et al. (2019) for field stars.
- Stars showing rich lithium content by the lithium absorption lines *or* stars showing rapid spectroscopic projected rotation rates are good candidates for young stars as shown by their cool kinematics.
- Stars with resolvable $v \sin i$ are almost certainly younger than 1 Gyr, and stars rotating faster than this detection limit have even younger 90% confidence upper limits on age.

- The ages derived from gyrochronologic models using $v \sin i$ are highly sensitive to the posterior uncertainty of $v \sin i$ near the detection limit; thus, showing the importance of careful spectral analysis and error modeling.

For further analysis, we are addressing whether the combination and rates of rotational spin-down and lithium depletion are the same in field stars versus open clusters as mentioned in section 5. We are also in the process of carefully extracting radial velocities and rotational velocities from the high-resolution spectra of the Kim et al. (2016) sample and their uncertainties. With this information, we will be able to further constrain the upper limits on age of field stars.

These ideas can further be explored using the large spectroscopic catalogs that are a result of exoplanet host star searches such as Keck. Many stars in spectroscopic catalogues are left unpublished due to the fact that broad spectral lines make it difficult to measure other aspects of the spectra such as radial velocity. Using the methods put forth in this thesis, we can use these spectra as a broad filter to confidently identify young stars based simply on their projected rotation rates and therefore we can identify young exoplanet host stars. This can open doors into learning more about planet migration as we now have a possible way of separating young and old planets and stars.

Acknowledgements

This work has made use of:

1. data from the European Space Agency (ESA) mission *Gaia*[3], processed by the *Gaia* Data Processing and Analysis Consortium (DPAC)[4]. Funding for the DPAC has been provided by national institutions, in particular the institutions participating in the *Gaia* Multilateral Agreement.

[3] https://www.cosmos.esa.int/gaia
[4] https://www.cosmos.esa.int/web/gaia/dpac/consortium

2. the NASA/IPAC Infrared Science Archive, which is funded by the National Aeronautics and Space Administration and operated by the California Institute of Technology.

I would like to thank my research advisor, Dr. Terndrup, for seeing my potential early on and giving me so many opportunities throughout the years of shuffling research projects. I would also like to thank Meredith and Collin for keeping me sane through the long hours of staring at screens during a pandemic and pointing out my many grammar mistakes.

I am grateful for the support from the Summer Undergraduate Research Program at The Ohio State University Department of Astronomy for kickstarting my project and providing training on writing and presenting scientific results; especially the support from Dr. Wayne Schlingman and Anna Voelker.

References

Almeida-Fernandes, F., & Rocha-Pinto, H. J. 2018, , 476, 184, doi: 10.1093/mnras/sty119

Angus, R., Beane, A., Price-Whelan, A. M., et al. 2020, , 160, 90, doi: 10.3847/1538-3881/ab91b2

Barnes, S. A. 2010, , 722, 222, doi: 10.1088/0004-637X/722/1/222

Bovy, J., Rix, H.-W., Hogg, D. W., et al. 2012, , 755, 115, doi: 10.1088/0004-637X/755/2/115

Brewer, J. M., Fischer, D. A., Valenti, J. A., & Piskunov, N. 2016, , 225, 32, doi: 10.3847/0067-0049/225/2/32

Buder, S., Lind, K., Ness, M. K., et al. 2019, , 624, A19, doi: 10.1051/0004-6361/201833218

Burke, C., Pinsonneault, M., State, A. S. O., & Univ., M. 2004, The Astrophysical Journal, 604, 272

Coker, C. T., Pinsonneault, M., & Terndrup, D. M. 2016, , 833, 122, doi: 10.3847/1538-4357/833/1/122

Denissenkov, P. A., Pinsonneault, M., Terndrup, D. M., & Newsham, G. 2010, , 716, 1269, doi: 10.1088/0004-637X/716/2/1269

Gallet, F., & Bouvier, J. 2013, , 556, A36, doi: 10.1051/0004-6361/201321302

Grieves, N., Ge, J., Thomas, N., et al. 2018, , 481, 3244, doi: 10.1093/mnras/sty2431

Johnson, D. R. H., & Soderblom, D. R. 1987, , 93, 864, doi: 10.1086/114370

Kawaler, S. D. 1988, , 333, 236, doi: 10.1086/166740

Keppens, R., MacGregor, K. B., & Charbonneau, P. 1995, , 294, 469

Kim, B., An, D., Stauffer, J. R., et al. 2016, , 222, 19, doi: 10.3847/0067-0049/222/2/19

Kraft, R. P. 1967, , 150, 551, doi: 10.1086/149359

Mackereth, J. T., Bovy, J., Leung, H. W., et al. 2019, , 489, 176, doi: 10.1093/mnras/stz1521

Mamajek, E. E., & Hillenbrand, L. A. 2008, , 687, 1264, doi: 10.1086/591785

McQuillan, A., Mazeh, T., & Aigrain, S. 2014, , 211, 24, doi: 10.1088/0067-0049/211/2/24

Meibom, S., Barnes, S. A., Latham, D. W., et al. 2011, , 733, L9, doi: 10.1088/2041-8205/733/1/L9

Moe, M., & Di Stefano, R. 2017, , 230, 15, doi: 10.3847/1538-4365/aa6fb6

Pinsonneault, M. 1997, , 35, 557, doi: 10.1146/annurev.astro.35.1.557

Pinsonneault, M. H., Terndrup, D. M., Hanson, R. B., & Stauffer, J. R. 2004, , 600, 946, doi: 10.1086/379925

Pourbaix, D., Tokovinin, A. A., Batten, A. H., et al. 2004, , 424, 727, doi: 10.1051/0004-6361:20041213

Raghavan, D., McAlister, H. A., Henry, T. J., et al. 2010, , 190, 1, doi: 10.1088/0067-0049/190/1/1

Simonian, G. V. A., Pinsonneault, M. H., & Terndrup, D. M. 2019, , 871, 174, doi: 10.3847/1538-4357/aaf97c

Simonian, G. V. A., Pinsonneault, M. H., Terndrup, D. M., & van Saders, J. L. 2020, , 898, 76, doi: 10.3847/1538-4357/ab9a43

Skumanich, A. 1972, , 171, 565, doi: 10.1086/151310

Soubiran, C., Jasniewicz, G., Chemin, L., et al. 2018, , 616, A7, doi: 10.1051/0004-6361/201832795

Spagna, A., Lattanzi, M. G., Re Fiorentin, P., & Smart, R. L. 2010, , 510, L4, doi: 10.1051/0004-6361/200913538

van Leeuwen, F., de Bruijne, J. H. J., Arenou, F., et al. 2018, Gaia DR2 documentation, Gaia DR2 documentation

Wu, Y., Xiang, M., Chen, Y., et al. 2021, , 501, 4917, doi: 10.1093/mnras/staa3949